High-throughput Growth of Microscale Gold Bicrystals for Single Grain Boundary Studies

Lucia T. Gan[†]*, Rui Yang*[†]*, Rachel Traylor, Wei Cai, William D. Nix, and Jonathan A. Fan**

[†]These authors contributed equally to this work

L. T. Gan, Dr. R. Yang, Dr. R. Traylor, Prof. J. A. Fan
Department of Electrical Engineering, Stanford University

Stanford, CA 94305, USA

Email: jonfan@stanford.edu

Dr. R. Yang

University of Michigan–Shanghai Jiao Tong University Joint Institute, Shanghai Jiao Tong University

Shanghai, China

Prof. W. Cai

Department of Mechanical Engineering, Stanford University

Stanford, CA 94305, USA

Prof. W. D. Nix

Department of Materials Science and Engineering, Stanford University

Stanford, CA 94305, USA

Keywords: bicrystals, crystal defects, grain boundaries, rapid melt growth

Abstract

The study of grain boundaries is foundational to understanding many of the intrinsic physical properties of bulk metals. Here, the preparation of microscale thin-film gold bicrystals, using rapid melt growth, is presented as a model system for single grain boundary studies. This materials platform utilizes standard fabrication tools and supports the high-yield growth of thousands of bicrystals per wafer, each containing a grain boundary with a unique <111> tilt character. The crystal growth dynamics of the gold grains in each bicrystal are mediated by platinum gradients, which originate from the gold-platinum seeds responsible for gold crystal nucleation. This crystallization mechanism leads to a decoupling between crystal nucleation and crystal growth, and it ensures that the grain boundaries form at the middle of the gold microstructures and possess a uniform distribution of misorientation angles. We envision that these bicrystals will enable the systematic study of the electrical, optical, chemical, thermal, and mechanical properties of individual grain boundary types.

Main Text

The intrinsic properties of metals are governed in part by grain boundaries, which are crystal defects at the interfaces between grains. Depending on the density and type of grain boundaries present, the same metallic materials can exhibit profoundly distinct characteristics. For example, the presence of grain boundaries greatly influences mechanical yield strength,[1] metal corrosion rates,[2] electrical conductivity,[3] and electromigration.[4] Important metal-catalyzed chemical reactions, such as carbon monoxide and carbon dioxide reduction, are enhanced by grain boundary density and

energetics.[5,6] In metal-based plasmonic devices, plasmon propagation length and electric field enhancements are strongly tied to the presence of grain boundaries.[7,8]

There is still an incomplete understanding of the properties of individual grain boundaries. This understanding is important for fundamental study, as the physical properties of bulk materials are described by the collective response of individual grains and their boundaries. Single grain boundaries are also relatively simple and well-defined, making them ideal systems for experimentalists and theorists to accurately corroborate experimental findings with analytic and numerical models.[9-12] The effect of single grain boundaries becomes particularly significant for metal structures scaling to the micro- and nanoscale, where many bulk material trends, such as grain boundary strengthening, break down.[13]

Bicrystals, formed from two adjacent metal crystals separated by a single grain boundary, are the standard for studying isolated grain boundaries. Historically, there are three main routes for preparing bicrystal metal structures: growing bicrystals from single crystal seeds,[14-16] welding two metal single crystals with polished facets through diffusion bonding,[17,18] and extracting microscopic bicrystals from polycrystals by focused ion beam milling.[19] All of these methods have proven to be powerful and controlled systems for studying grain boundary properties, but they also feature some nonidealities. In all cases, the bicrystals can only be produced one at a time, making the realization of large quantities of bicrystals extremely labor intensive. The first and second methods cannot readily scale down to micro- or nanoscale dimensions. Novel extensions of these methods have enabled the growth of bicrystals with continuously varying grain boundary structures,[20] but these preparations are currently limited to centimeter-scale structures.

In this paper, we introduce the experimental preparation of microscale gold bicrystals on an amorphous insulator, via metal-on-insulator rapid melt growth, as a new paradigm for defect engineering. Compared to existing metal bicrystal preparation methods, our technique exhibits a number of advantageous features. First, it is a high-throughput, high-yield crystal growth process that can produce many thousands of gold bicrystals on a silicon dioxide substrate in parallel, each with a unique <111> tilt character. Thus, exhaustive structure-property investigations within this important grain boundary parameter space can be performed in a comprehensive manner. Second, our sample preparation process uses standard lithographic patterning and fabrication tools, namely a rapid thermal annealer for rapid melt growth processing. Maskless lithography provides a straightforward and fast way to customize the bicrystal designs and form factors. Suspended metal bicrystal structures can also be readily prepared by undercutting the substrate with wet or vapor etching to isolate the bicrystal, which is useful for transmission electron microscopy (TEM) or mechanical testing preparation. Third, the wire-like form factor of the microstructures and their growth on an inert, low-refractive index substrate enables the direct study of electronic, optical, chemical, and thermal properties of single grain boundaries.

Bicrystal preparation and characterization

The bicrystal fabrication process is outlined in **Figure 1** and builds on the rapid melt growth technique our group developed for realizing single crystal metal-on-insulator microstructures.[21] The complete fabrication procedure is detailed in Figure S1 and the Experimental Section. A lithography and lift-off process are used to define polycrystalline gold stripes, along with polycrystalline platinum seeds at the opposing ends of each stripe, on a thermally-oxidized silicon wafer (step 1, Figure 1a). The as-deposited gold and platinum grains are (111)-textured normal to the wafer and have random

in-plane orientations ranging from <110> to <112>, consistent with the known texturing of vapor-deposited face-centered cubic (fcc) metallic films on amorphous substrates.[21,22]

The metal structures are then encapsulated in a crucible of amorphous silicon dioxide and heated with a rapid thermal annealing system to a peak temperature of 1080˚C, which is above gold's melting temperature of 1064˚C (step 2, Figure 1a). During heating, solid state diffusion occurs in regions of the seed in the thickness direction where the gold overlaps with the platinum, forming an alloy.[21] Since platinum forms an isomorphous binary phase diagram with gold, in which the liquidus and solidus temperatures both increase with platinum content, the resulting gold-platinum alloy is a solid throughout the entire annealing process.[21] Thus, the platinum-gold seed remains solid while the gold stripe melts to the liquid phase at the peak temperature.

As the temperature drops below the melting point for gold on cooling, a single grain in the alloyed seed region serves as the site for liquid epitaxial growth, driving a solidification front that propagates from each seed towards the center of each stripe (step 3, Figure 1a), yielding a bicrystal. After cooling to room temperature, plasma etching of the overlying silicon dioxide capping layer exposes the gold bicrystals (step 4, Figure 1a). The temperature processing cycle for the entire annealing and crystallization procedure is summarized in Figure 1b and takes just over two minutes.

A scanning electron microscope (SEM) image and electron backscatter diffraction (EBSD) maps of a representative bicrystal clearly delineate two single crystal gold grains separated by a well-defined grain boundary (Figure 1c). Each gold grain remains (111)-textured normal to the wafer and possesses a different in-plane crystal orientation. This results in an isolated <111> tilt grain boundary, where the lattice rotation axis is parallel to the boundary plane. The EBSD images also

reveal that the seed region remains polycrystalline. This growth technique eliminates the need for using a large-scale single crystal seed material and, thus, simplifies the fabrication process. The seed's polycrystallinity plays a key role in the scalability of our platform: since a single grain with random orientation dictates the bicrystal's grain orientation, a wide range of tilt grain boundary structures are produced in a single annealing experiment. In addition, bicrystal formation occurs only when the peak temperature exceeds gold's melting temperature, which is corroborated by experiments where the structures are heated to a peak temperature of 900˚C, using the same 15°C per second heating and cooling parameters described in Figure 1b. While grain growth does occur, these stripes remain polycrystalline after cooling (Figure S2). This indicates that the bicrystals are not a result of grain growth and only form after gold is in the liquid phase.

We examine the grain boundaries at atomic scale resolution using high resolution scanning transmission electron microscopy (HRSTEM). To prepare a top-view TEM sample, we fabricate suspended bicrystals by undercutting the underlying oxide substrate with HF vapor etching (Figure 1d), stabilizing the thin film structure with a platinum-deposited frame, and then lifting out the bicrystal (Figure S3). This sample preparation method is enabled by our unique metal-on-insulator system. A top-view HRSTEM analysis confirms the common <111> zone axis across the tilt grain boundary (Figure 1e). The grain boundary plane is not perfectly on zone, resulting in a Moiré pattern at the boundary region, which is denoted by the purple region in Figure 1e. A Fourier transform of the image, shown in the inset, clearly elucidates the misorientation angle between grains. A standard side-view TEM cross-section reveals horizontal lattice fringes across the grain boundary parallel to the metal-oxide interface, corresponding to (111) planes (Figure 1f).

Large area EBSD orientation maps display a high yield of bicrystals of varying lengths exhibiting a diversity of <111> tilt grain boundaries near the middle of each stripe (**Figure 2**a). Of the 247 samples investigated, 246 stripes formed into bicrystals following the annealing treatment, resulting in over 99% bicrystal yield. Out of these 246 bicrystals, only one did not form with the expected <111> z-axis orientation, resulting in over 99% yield of <111> tilt grain boundaries.

Notably, the distribution of misorientation angles is relatively uniform from 0˚ to 60˚ for the investigated bicrystals, where the maximum misorientation angle is limited due to the face-centered cubic symmetry. The misorientation angle distribution, plotted as a cumulative distribution function (cdf) in Figure 2b, compares well with a uniform cdf. The uniform distribution of tilt grain boundary angles in our bicrystals is attributed to the gold grains having uniformly distributed and uncorrelated in-plane orientations from <110> to <112>, as shown in the inverse pole figures and crystal orientation distribution in Figure 2c-d. The appearance of a full range of <111> tilt misorientation angles in our system is quantitatively different from the grain boundary angle distributions in annealed polycrystalline fcc thin-film samples. In polycrystalline fcc systems, large angle grain boundaries typically transform into energetically preferred coincidence site lattice (CSL) boundaries during annealing, specifically the Σ7 (38˚) and Σ3 (60˚) boundaries that contain a high density of coinciding lattice points.[23] As such, our bicrystal preparation method is particularly well suited for the realization and study of all grain boundary angles that can exist in vapor-deposited (111)-textured fcc films.

Unexpectedly, we observe that the grain boundaries form selectively in the center of each bicrystal. The relative boundary positions from 246 bicrystals after two hours of post-annealing at 700˚C, with lengths ranging from 40 μm to 160 μm, are displayed in **Figure 3**a. The narrow normal

distribution centered around the halfway point of the stripes suggests that the rate of solidification front growth perpendicular to the <111> axis is independent of crystallographic orientation. This observation is contrary to established trends in fcc grain growth, in which the growth rate of certain grain orientations that minimize surface and interface energies are dominant during annealing. For example, annealing experiments of fcc metal foils demonstrate that the growth rates of {111}<112> grains dominate.[24] Similarly, annealed polycrystalline gold thin films exhibit preferential growth of {111}<112> and {111}<110> grains.[23] In applying these trends to our bicrystals, one would expect certain grain orientations to grow faster than others, resulting in grain boundary positions far from the middle of the stripe.

We deduce that the thermodynamic forces driving crystallization are dictated not only by crystal growth kinetics, but by small amounts of platinum doping in the gold microstructures during crystal growth. Evidence for this crystal growth mechanism is obtained by characterizing the platinum concentration using Nanoscale Secondary Ion Mass Spectrometry (NanoSIMS), which is a highly sensitive compositional analysis technique. With this tool, the platinum composition in the bicrystal samples is qualitatively analyzed by sputtering the sample surface with a focused cesium ion beam and measuring ejected secondary platinum-194 ions with a mass spectrometer. Figure 3b reveals a long-range platinum gradient along the length of the bicrystal, where the concentration of platinum is the highest nearest the seeds, decreases towards the grain boundary, and is minimal near the middle of the stripe.

This platinum gradient imposes a gradient in solidus temperature along the gold stripe, as evidenced in the binary phase diagram (Figure 3c). Consequently, as the gold melt cools, the regions of the stripe containing the highest platinum levels (i.e., regions near the seed) solidify first. As the

system continues to cool, a directional solidification front moves from the seeds towards the center of the stripe. Since the platinum seed-gold stripe is geometrically symmetric, the platinum gradient is also symmetric across the stripe and the grain boundary forms at the stripe middle, independent of the crystal orientation of the gold grains.

Platinum doping in the gold arises when the gold liquefies and small amounts of platinum leach out from the seed into the gold. The seed serves as a reservoir for a platinum concentration gradient, which forms quickly upon gold liquefaction. We also use NanoSIMS to characterize the concentration of platinum in devices that are annealed to a peak temperature of 900˚C, which is below the melting point of gold, to probe the diffusion behavior of platinum in solid gold. These samples do not exhibit any discernable platinum concentration or gradient in the gold stripe (Figure S4), which is consistent with established diffusion lengths of platinum in solid gold.[25] This indicates that the long-range platinum gradient in the bicrystals forms when the gold is in the liquid phase.

Grain boundary energy mapping

The high-throughput nature of our preparation platform provides a facile method for studying fundamental metallurgical properties of grain boundaries. As a simple demonstration, we utilize our bicrystal system to map grain boundary energy as a function of misorientation angle. The experimental extraction of these properties in (111)-textured fcc films is inherently statistical and requires the preparation and characterization of a large quantity of many grain boundary types, which is well within the scope of our sample preparation method. In contrast, bicrystal-based grain boundary studies prepared using conventional means are limited to a small number of samples, due to the labor-intensive nature of sample preparation.[18,26-28] Our method is complementary to

experimental studies based on bulk polycrystalline fcc metal systems at thermal equilibrium, and intrinsically possesses a large density of varying grain boundary structures in (111)-textured fcc films.

Grain boundary energy itself cannot be directly measured and must be probed using energy balance equations. As an example, grain boundary energy can be estimated by using atomic force microscopy (AFM) measurements of surface groove angles that form in polycrystals where grain boundaries intersect the surface.[29] To equilibrate the surface excess free energies and the grain boundary energies, surface diffusion occurs, which leads to the groove formation. Grain boundary energy is related to the surface energy and the dihedral angle formed by the surface grooves, expressed in Equation 1, where γ_{gb} is the grain boundary energy, γ_s is the surface free energy, and α is the dihedral angle.

$$\frac{\gamma_{gb}}{\gamma_s} = 2\cos\frac{\alpha}{2} \quad (1)$$

Our bicrystals' unique geometry allows us to complement this method using electron microscopy. Similar to polycrystals, our bicrystals form surface grooves normal to the substrate, seen in the side-view TEM cross-section image (Figure 3d and S5). In addition, cusps also form in-plane due to the microscale form factor and are readily viewed from SEM imaging (Figure 3e). Therefore, the dihedral angles are directly measured through electron microscopy, and Equation 1 can relate the measured angles to grain boundary energy. With direct readout of the dihedral angles and the misorientation from SEM and EBSD images of large quantities of bicrystals, we can compute the grain boundary energy in gold thin films in a relatively rapid manner from a large dataset uniformly covering the entire range of misorientation angles. Energy statistics were taken from 245 bicrystals.

In this study, we measured the same grain boundaries that were used in Figure 2 for misorientation statistics, except for one bicrystal that did not form a <111> tilt boundary.

The mean relative grain boundary energy as a function of misorientation angle is given by the solid line in Figure 3f (full dataset included in Figure S6), where the shaded regions correspond to one standard deviation from the mean. The local minima at 38˚ and 60˚ correspond to low CSL Σ7 boundaries and Σ3 twin boundaries, respectively. The energy-misorientation profile matches well with atomistic simulations of gold <111> tilt boundaries.[9-11]

This technique still has a number of sources of error. First, Equation 1 is a simplified equation that applies to crystals that are symmetric about the boundary, and it neglects higher order terms that address the influence of boundary asymmetry on energy. Second, other internal forces such as elastic strain energies may modify the energy balance.[22] Lastly, the platinum impurities that exist across the stripes may increase the anisotropy of gold's surface energy, which influences grain boundary energy.[30,31] The large number of samples mitigate some of the error imposed by these sources, but can be further improved by fabricating larger structures, engineering the platinum gradient, and investigating strain.

Extending the growth platform

Since the grain boundaries are entirely specified through the seed-stripe geometry, a broad range of multi-grain configurations can be produced through photolithography. Triple junctions are specified by patterning Y-shaped gold microstructures with three platinum seeds at distal ends (**Figure 4**a). Through geometrical symmetry, the resulting platinum distribution in the gold melt

during crystal growth will be a minimum at the center of the Y shape, driving the formation of triple points, relevant for thin film electromigration studies.[32]

Furthermore, gold structures possessing multiple grain boundaries with a bamboo-like microstructure can be prepared by lithographically defining branches with multiple seeds (Figure 4b). Such bamboo-type grain morphologies are the basis for electrical interconnects in integrated circuits, where continuous grain boundary diffusion paths do not exist. These bamboo microstructures are difficult to fabricate through conventional annealing,[33] making our structures very relevant for studies in mass transport mechanisms at grain boundaries in interconnects.

Conclusion

In summary, we report a high-throughput and high-yield approach for producing gold bicrystal microstructures, which enables the systematic study of the full parameter space of gold <111> tilt grain boundaries that exist in vapor-deposited fcc films. The grain boundary misorientations are uniformly distributed between 0˚ to 60˚, which is quantitatively different from polycrystalline systems. Notably, our bicrystal growth mechanism is driven primarily by a platinum gradient profile that arises during melt, resulting in the highly predictable positioning of the grain boundary. The unique wire-like form factor of the microscale bicrystals introduces a complementary method for investigating fundamental material properties such as grain boundary energy. Our preparation process using standard lithography and fabrication tools, coupled with the platinum-mediated crystal growth mechanism, allows us to extend our platform beyond bicrystals. For example, complex geometries such as bamboo-type polycrystals, which are very relevant to many electrical studies, can be readily defined with our method.

This study paves the way for fundamental studies and applications of individual grain boundaries. The metal-on-oxide microstructures enable the study of electronic, optical, mechanical, catalytic, and thermal properties of single grain boundaries. The bicrystal growth platform can potentially be further extended to the growth of non-(111)-textured thin-films in gold and other fcc metal materials, opening the door for the systematic investigation of the entire parameter space for fcc metal grain boundaries.

Experimental Section

Fabrication: 300 nm of thermal oxide layers were grown at 1050˚C on (100) single crystal p-type silicon wafers. Photolithography with a 1-µm-thick positive photoresist (Shipley 3612) was performed using a direct write lithography tool (Heidelberg MLA 150) to pattern the seeds. After photoresist development, a 2-nm-thick titanium adhesion layer and a 30-nm-thick platinum metal film were deposited using electron beam evaporation (AJA E-Beam Evaporation System). The sample was soaked in acetone for metal lift-off. The platinum seeds were 10 µm long and 10 µm wide. A second lithography step was used for patterning the gold stripes. After development, a 100-nm-thick gold metal film was deposited using electron beam evaporation, again followed by soaking in acetone for metal lift-off. The gold stripes had lengths ranging from 40 to 160 µm and widths of 4 µm. The stripes overlapped the seeds lengthwise by 3 µm. Following metal deposition, 3 µm of low-pressure chemical vapor deposition (LPCVD) silicon dioxide encapsulation layers were grown at 400˚C. The wafers were heated using rapid thermal annealing (All-Win 610 Rapid Thermal Process System) and the temperatures in the furnace were controlled using a pyrometer. The samples were heated with a ramp rate of 15˚C/s up to 1080˚C, held for 1 second, and cooled with a ramp rate of 15˚C/s. After annealing, the oxide cap was removed through dry reactive plasma etching (Versaline

LL-ICP Oxide Etcher). Suspended bicrystals were fabricated by undercutting the silicon dioxide substrate through HF vapor etching after patterning large gold contact pads as anchors (SPTS uEtch).

Characterization: The SEM and EBSD images were collected using a FEI Magellan 400 XHR Scanning Electron Microscope equipped with a Bruker Quantax e-Flash(HR) EBSD detector and a FEI Strata 235DB dual-beam Focused Ion Beam Microscope. The SEM images detailing the liftout process were collected using a FEI Helios G4 UX dual-beam Focused Ion Beam Microscope. The HRSTEM images were collected using the TEAM I double-aberration-corrected scanning transmission electron microscope located at the National Center for Electron Microscopy, Molecular Foundry, Lawrence Berkeley National Laboratory. NanoSIMS analysis was performed using a Cameca NanoSIMS 50L with the spot size specified by the D1 = 2 aperture. The primary ion current was 12.05 pA.

Supporting Information

Supporting Information is available from the Wiley Online Library or from the author.

Acknowledgements

L.T.G. and R.Y. contributed equally to this work. The authors thank C. Hitzman for his contributions to the NanoSIMS experiments and J. Ciston for TEM support. This work was supported by the National Science Foundation under Award 1804224. Part of this work was performed at the Stanford Nanofabrication Facility and the Stanford Nano Shared Facilities, supported by the National Science Foundation under award ECCS-1542152. Work at the Molecular Foundry was supported by the Office of Science, Office of Basic Energy Sciences, of the U.S. Department of Energy under Contract No. DE-AC02-05CH11231. R. Y. acknowledges support from Shanghai Sailing Program under award 19YF1424900, and from University of Michigan–Shanghai Jiao Tong University Joint Institute in Shanghai Jiao Tong University.

Received: ((will be filled in by the editorial staff))
Revised: ((will be filled in by the editorial staff))
Published online: ((will be filled in by the editorial staff))

References

[1] N. Hansen, *Scr. Mater.* **2004**, *518*, 801.

[2] A. King, G. Johnson, D. Engelberg, W. Ludwig, J. Marrow, *Science* **2008**, *321*, 382.

[3] K.-H. Koo, K. C. Saraswat, *Study of Performances of Low-k Cu, CNTs, and Optical Interconnects* in *Nanoelectronic Circuit Design* (Eds: N. Jha, D. Chen), Springer, New York, NY, USA **2011**.

[4] D. G. Pierce, P. G. Brusius, *Microelectron. Reliab.* **1997**, *37*, 1053.

[5] C. W. Li, J. Ciston, M. W. Kanan, *Nature* **2014**, *508*, 504.

[6] R. G. Mariano, K. McKelvey, H. S. White, M. W. Kanan, *Science* **2017**, *358*, 1187.

[7] H. Ditlbacher, A. Hohenau, D. Wagner, U. Kreibig, M. Rogers, F. Hofer, F. R. Aussenegg, J. R. Krenn, *Phys. Rev. Lett.* **2005**, *95*, 257403.

[8] J.-S. Huang, V. Callegari, P. Geisler, C. Brüning, J. Kern, J. C. Prangsma, X. Wu, T. Feichtner, J. Ziegler, P. Weinmann, M. Kamp, A. Forchel, P. Biagioni, U. Sennhauser, B. Hecht, *Nat. Commun.* **2010**, *1*, 150.

[9] D. Wolf, *Acta Metall. Mater.* **1990**, *38*, 781.

[10] V. V. Bulatov, B. W. Reed, M. Kumar, *Acta Mater.* **2014**, *65*, 161.

[11] B. Runnels, I. J. Beyerlein, S. Conti, M. Ortiz, *J. Mech. Phys. Solids* **2016**, *94*, 388.

[12] G. C. Hasson, C. Goux, *Scr. Metall.* **1971**, *5*, 889.

[13] J. R. Greer, J. T. M. De Hosson, *Prog. Mater. Sci.* **2011**, *56*, 654.

[14] K. V. Gow, B. Chalmers, *Br. J. Appl. Phys.* **1951**, *2*, 300.

[15] B. Chalmers, *Can. J. Phys.* **1953**, *31*, 132.

[16] R. A. Marks, S. T. Taylor, E. Mammana, R. Gronsky, A. M. Glaeser, *Nat. Mater.* **2004**, *3*, 682.

[17] T. Schober, R. W. Balluffi, *Philos. Mag.* **1969**, *20*, 511.

[18] H. Yoshida, K. Yokoyama, N. Shibata, Y. Ikuhara, T. Sakuma, *Acta Mater.* **2004**, *52*, 2349.

[19] N. Kheradmand, H. Vehoff, *Adv. Eng. Mater.* **2012**, *14*, 153.

[20] L. G. Ware, D. H. Suzuki, K. R. Wicker, Z. C. Cordero, *Scr. Mater.* **2018**, *152*, 98.

[21] K. Zhang, X. B. Pitner, R. Yang, W. D. Nix, J. D. Plummer, J. A. Fan, *Proc. Natl. Acad. Sci. U. S. A.* **2018**, *115*, 685.

[22] C. V. Thompson, *Annu. Rev. Mater. Sci.* **2000**, *30*, 159.

[23] P. Parajuli, R. Mendoza-Cruz, U. Santiago, A. Ponce, M. J. Yacamán, *Cryst. Res. Technol.* **2018**, *53*, 1800038.

[24] S. Jin, M. Huang, Y. Kwon, L. Zhang, B.-W. Li, S. Oh, J. Dong, D. Luo, M. Biswal, B. V. Cunning, P. V. Bakharev, I. Moon, W. J. Yoo, D. C. Camacho-Mojica, Y.-J. Kim, S. H. Lee, B. Wang, W. K. Seong, M. Saxena, F. Ding, H.-J. Shin, R. S. Ruoff, *Science* **2018**, *362*, 1021.

[25] M. Hansen, K. Anderko, H. W. Salzberg, *J. Electrochem. Soc.* **1958**, *105*, 260C.

[26] J. F. Shackelford, W. D. Scott, *J. Am. Ceram. Soc.* **1968**, *51*, 688.

[27] X. R. Qian, Y. T. Chou, *Philos. Mag. A* **1982**, *45*, 1075.

[28] Y. T. Chou, B. C. Cai, A. D. Romig Jr, L. S. Lin, *Philos. Mag. A* **1983**, *47*, 363.

[29] L. E. Murr, *Interfacial phenomena in metals and alloys*, Addison-Wesley, Reading, MA, USA **1975**.

[30] D. Chatain, P. Wynblatt, G. S. Rohrer, *Acta Mater.* **2005**, *53*, 4057.

[31] E. D. Hondros, D. McLean, *Philos. Mag.* **1974**, *29*, 771.

[32] R. Rosenberg, M. Ohring, *J. Appl. Phys.* **1971**, *42*, 5671.

[33] K. N. Tu, *J. Appl. Phys.* **2003**, *94*, 5451.

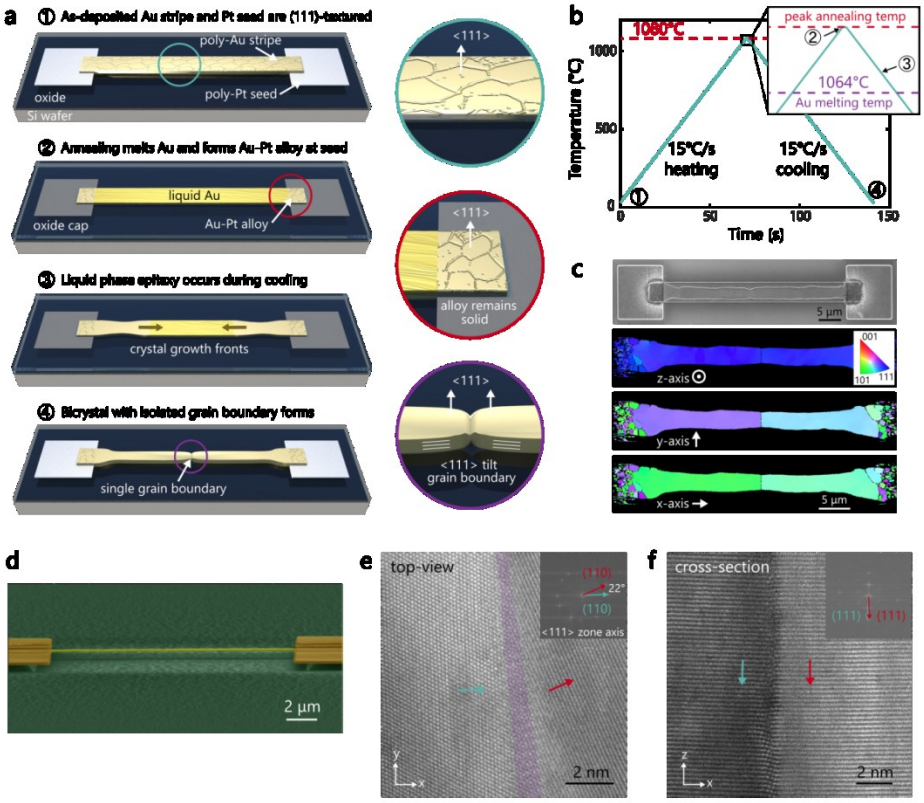

Figure 1. Bicrystal preparation and characterization. a) Schematic illustrations of the bicrystal growth process. (1) Polycrystalline gold stripes and polycrystalline platinum seeds are deposited on a thermally-oxidized silicon wafer; the as-deposited gold and platinum grains are (111)-textured normal to the wafer (inset). (2) The metal structures are encapsulated in a silicon dioxide crucible and annealed; the seed region forms into a gold-platinum alloy that remains solid throughout annealing (inset). (3) During cooling, liquid epitaxial growth fronts propagate from each seed towards the center of each stripe. (4) The annealing treatment results in bicrystals; each bicrystal possesses an isolated <111> tilt grain boundary (inset). b) Plot of the annealing recipe for the rapid melt growth process. c) SEM image and EBSD maps of a representative bicrystal, which clearly delineate two single crystal gold grains separated by a well-defined grain boundary. The EBSD maps show the crystal directions that are parallel to the z-, y-, and x-axis in the sample, respectively, which are indicated by the arrows. d) False-colored SEM image of a suspended bicrystal prepared by undercutting the oxide substrate. e) Top-view HRSTEM image confirms a common <111> zone axis across the grain boundary. The purple region indicates the grain boundary plane, which is not perfectly aligned with the zone axis. The Fourier transform indicates a 22˚ grain boundary misorientation (inset). f) Side-view TEM cross-section reveals (111) lattice fringes.

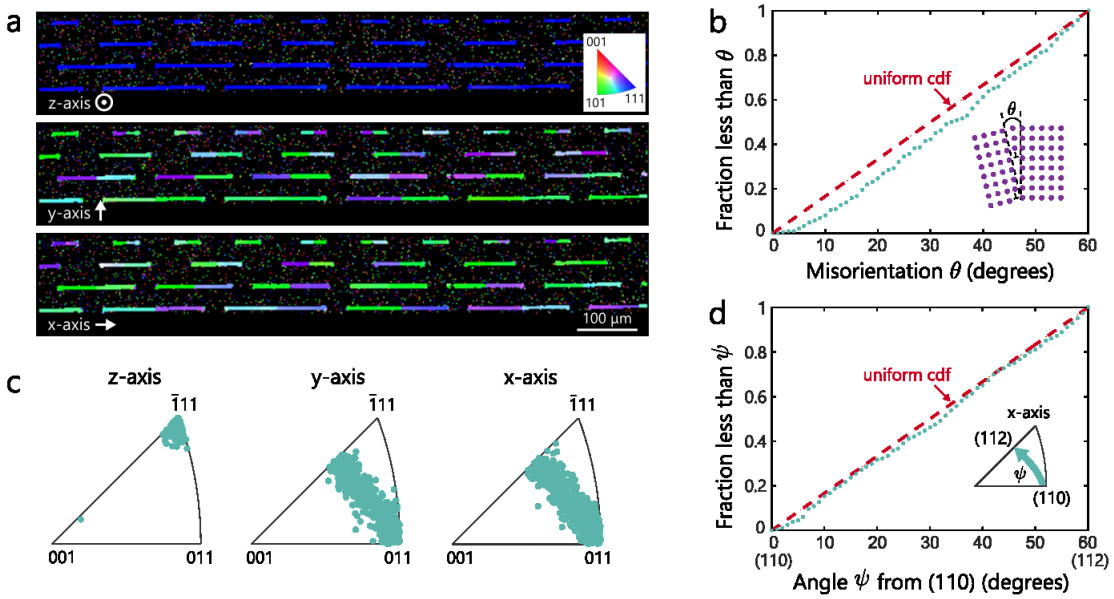

Figure 2. Statistics of grain orientations in bicrystal gold prepared by the high-throughput, high-yield growth technique. a) Large-area EBSD maps in the z-, y-, and x-sample-axes display a diversity of bicrystals of varying lengths with <111> tilt grain boundaries. b) Plot of grain boundary misorientation angle distribution showing that the misorientation angles are uniformly distributed. c) Inverse pole figures show the distribution of crystal directions parallel to the z-, y-, and x-axis in the sample, respectively. Grains are (111)-textured in the z-direction and randomly oriented in-plane from <110> to <112>. The sample axis directions are indicated by the arrows in a). d) Plot of x-axis grain orientation distribution showing that the grain orientations are uniformly distributed between <110> and <112>. Statistics are taken from 246 bicrystals.

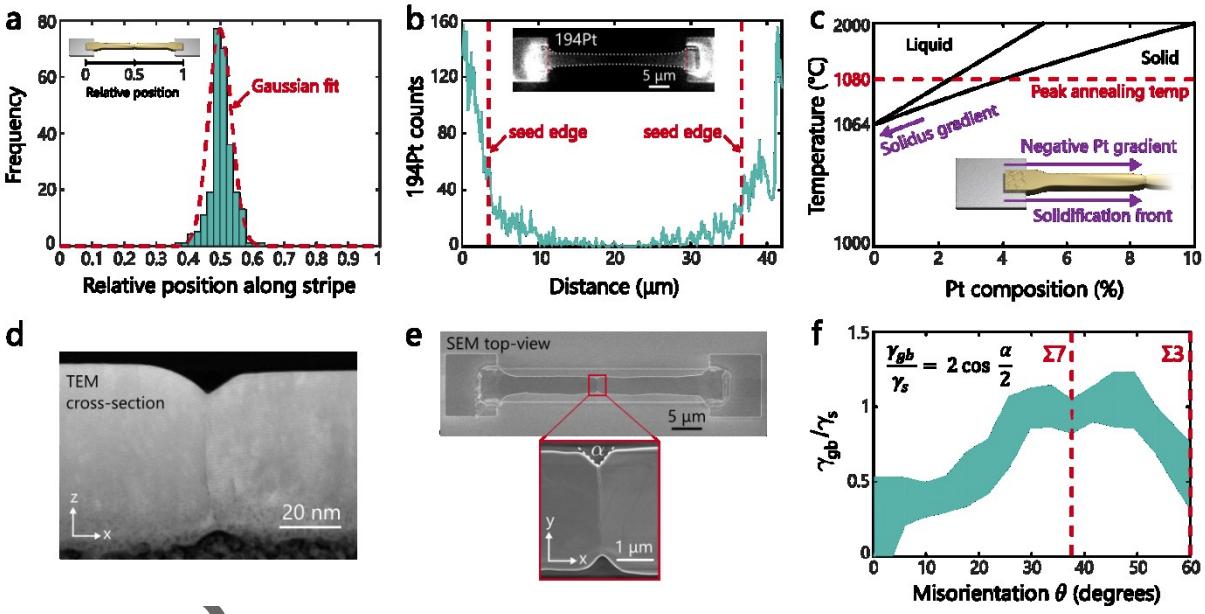

Figure 3. Bicrystal growth mechanism and grain boundary energy mapping. a) Statistics of grain boundary position show that grain boundaries form selectively near the center of each bicrystal. b) NanoSIMS compositional analysis reveals a distinct platinum gradient across the stripe. c) Phase diagram shows that the negative platinum gradient creates a spatial gradient in the melting (solidus) temperature that mediates the propagation of a solidification front originating from the seed. For symmetric bicrystal structures, solidification fronts propagating from each seed meet at the center of the gold stripe, where there is a minimum in the platinum concentration. d) Side-view TEM cross-section and e) top-view SEM showing surface grooves at the grain boundary. α indicates the in-plane dihedral angle. f) Plot of the mean relative grain boundary energy γ_{gb}/γ_s as a function of misorientation angle ϑ is given by the solid line. Shaded regions correspond to one standard deviation from the mean. Local minima correspond to lower energy Σ7 and Σ3 CSL boundaries. Statistics are taken from 245 bicrystals.

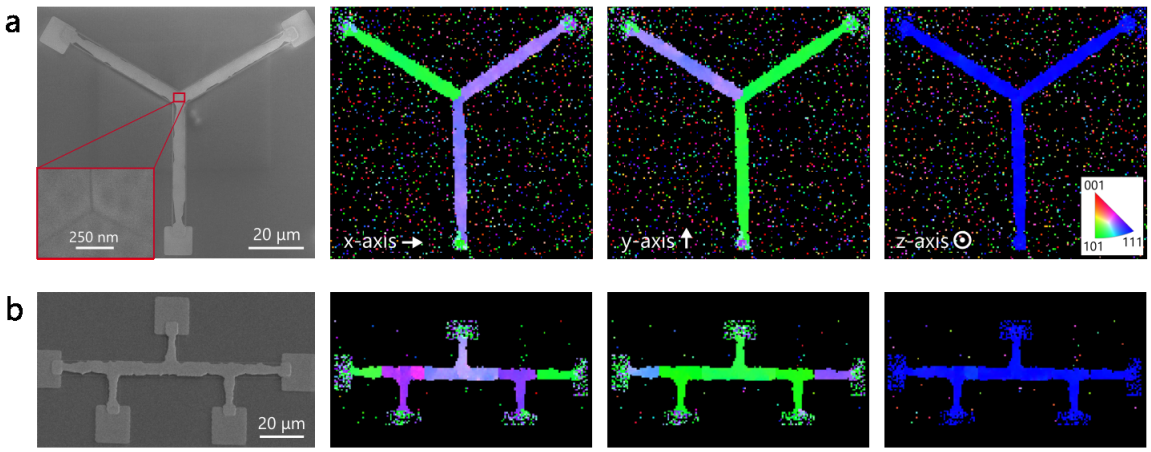

Figure 4. Preparation of tricrystals and bamboo-like morphologies that extend the growth platform beyond bicrystals. a) SEM image and EBSD maps in the z-, y-, and x-sample-axes for tricrystals, which are specified by Y-shaped microstructures; the platinum-mediated crystal growth process drives the formation of a triple junction (inset). b) SEM image and EBSD maps in the z-, y-, and x-sample-axes for bamboo-like gold interconnects prepared by defining branches with multiple seeds.

Single grain boundary studies are enabled through the preparation of microscale gold bicrystals via rapid melt growth. This materials platform supports the high-throughput and high-yield growth of gold bicrystals on amorphous oxide. Crystallization is mediated by platinum doping, which decouples crystal nucleation from growth. These bicrystals offer model systems for the systematic study of individual defect properties.

Keyword: grain boundaries

L. T. Gan, R. Yang, R. Traylor, W. Cai, W. D. Nix, and J. A. Fan*

High-throughput Growth of Microscale Gold Bicrystals for Single Grain Boundary Studies